

## RELATIONSHIP BETWEEN FOURIER-MODES AND SPATIAL-STRUCTURES IN A CAVITY - BOUNDARY LAYER INTERACTION AT MODERATE REYNOLDS NUMBERS.

\*F. Lusseyran, \*A. Rambert, \*P Gougat, \*Yann Fraigneau, \*\*A. Elcafsi ,\*\*\*G. Quénot,

\*LIMSI-CNRS B. P. 133 91403 Orsay, \*\*FST, Campus Universitaire 1060 Tunis , Tunisie,

\*\*\* CLIPS-IMAG, BP53, 38041 Grenoble

### ABSTRACT

The dynamic behaviour of the vortex structures occurring in a cavity in interaction with a boundary layer controls the flow confinement inside the cavity. The vortex structures present small scales as well as large scales related to the cavity geometry. These eddies are usually non-stationary. One of main applications of this study concerns the pollutant dispersion within an urban street canyon when ambient winds aloft are perpendicular to the street. Experimental and numerical characterisations of the vortex structures are developed at moderate Reynolds numbers. The results concern low velocities close to the laminar-turbulent transition of the outside flow, for a given geometry of cavity  $H/L = 0.5$ . Flow velocity measurements inside and outside the cavity are performed by Laser Doppler Velocimetry and Particle Image Velocimetry based on the Optical Flow method. The Reynolds number, based on the height of cavity, is close to 3000 for the simulation and PIV measurements and ranging between 2000 and 8000 for LDV measurements.

2D direct numerical simulations are obtained from a code solving Navier-Stokes equations (code OLORIN developed at LIMSI) for unsteady isothermal incompressible flow. Equations are discretized following a finite volumes approach with schemes of order 2 in space and time. The flow is computed for the same geometrical and hydrodynamic conditions as the experimental ones.

The interaction between a flow and a cavity is a test configuration for confrontations between numerical simulation and experiments. However a quantitative confrontation "step by step" makes no sense in the case of a non-stationary, non-linear and therefore unpredictable problem. We propose a first simple approach comparing temporal and spatial modes.

For  $U_\infty < 1.4 m/s$  measurements and simulation show the existence of three main frequency modes, quantitatively in very good agreement. Measurements of the velocity fields by 2D PIV, associated with 2D visualisations show the existence of instabilities in the shear layer at the boundary between cavity and the main stream. One notes that the vertical velocity component  $\mathbf{v}$  grows apparently linearly after the upstream edge of the cavity. The fit of the evolution of  $\mathbf{v}$  according to  $x$  with a physical description of instability growth, afford us to measure spatial amplification rate and wavelength. The spatial modes properties obtained from the experimental velocity field and the numerical one, again are in very good agreement.

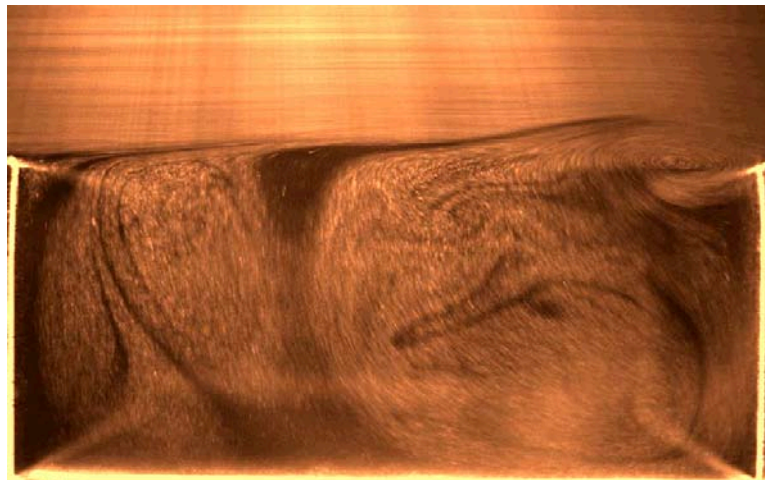


**Figure 1 :** Visualisation of the flow above and in the cavity, obtained using a laser light sheet and a seeding of the air by smoke.

## INTRODUCTION

The dynamic behaviour of the vortex structures occurring in a cavity in interaction with a boundary layer controls the flow confinement inside the cavity. The vortex structures present small scales as well as large scales related to the cavity geometry. These eddies are usually non-stationary. One of the main applications of this study concerns the pollutant dispersion within an urban street canyon when ambient winds aloft are perpendicular to the street. Experimental and numerical characterisations of the vortex structures are developed at moderate Reynolds numbers. The results presented concern low velocities close to the laminar-turbulent transition of the outside flow, for a given geometry of cavity  $H/L = 0.5$ . Flow velocity measurements inside and outside the cavity are performed by Laser Doppler Velocimetry and Particle Image Velocimetry based on the Optical Flow method. The Reynolds number, based on the height of cavity, is close to 3000 for the simulation and PIV measurements and ranging between 2000 and 8000 for LDV measurements. 2D direct numerical simulations are obtained for the same geometrical and hydrodynamic conditions as the experimental ones.

The interaction between a flow and a cavity is a test configuration for confrontations between numerical simulation and experiments. However a quantitative confrontation "step by step" makes no sense in the case of a non-stationary, non-linear and therefore unpredictable problem. We propose a first simple approach comparing temporal and spatial modes.

## EXPERIMENTAL CONDITIONS

The configuration of the studied cavity in interaction with boundary layer is recalled Figure 2 [Rambert 2000]. The time-frequency analysis uses the time records of the horizontal velocity component, measured using a laser Doppler anemometer (LDV:Aerometrics RSA). The mean flying time between the oil particles is of  $9 \cdot 10^{-4}$ s and the time of record of 150s. The power spectral density is estimated via Welch's method with overlapping, leading to a spectral resolution of 0.244Hz.

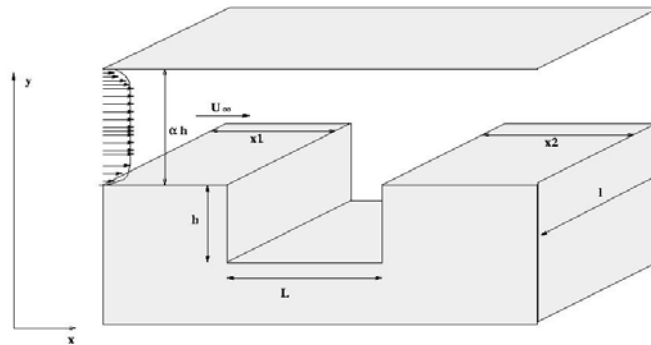


**Figure 2 :** Schema of the testing bench: The cavity dimensions are  $L = 0.1m$ ,  $l = 0.3m$ ,  $h = 0.05m$

The Particle Image Velocimetry based on Optical Flow offers a new approach for analysing flow images. It largely improves spatial accuracy and minimises the number of spurious vectors. Optical flow computation consists in extracting a dense velocity field from an image sequence assuming that the intensity is conserved during the displacement. Several techniques have been developed for the computation of optical flow. The technique that was chosen for PIV application was introduced by Quénot (1999) as Orthogonal Dynamic Programming algorithm for optical flow detection from a pair of images. Compared with the classical PIV method, the optical flow has the following advantages: (i) it can be applied simultaneously to sequences of more than two images; (ii) it performs a global image match by enforcing continuity and regularity constrains on the flow field. This helps in ambiguous or low particle density regions; (iii) It provides dense velocity fields (iiii) local correlation is iteratively searched for in regions whose shape is modified by the flow, instead of being searched by fixed windows. This greatly improves the accuracy in regions with strong velocity gradients. A sequence of 300 image pairs is recorded by a digital camera (Pulnix 9701, 30 images/s, 768x484 pixels, gray dynamics of 8 bits). The time between two images is 10 ms and the air is seeded with smoke. The aspect ratio of the cavity is kept constant ( $h/L = 0.5$ ), therefore the control parameter is the flowrate  $U_\infty$ , which varies from 0.6m/s to 4.5m/s for the LDV measurements.  $U_\infty = 0.85m/s$  for the analysis of the spatial structures of the flow from PIV snapshots.

## NUMERICAL SIMULATION

### Governing equations

We have carried out several 2D numerical simulations performed with a code solving Navier-Stokes equations for unsteady isothermal incompressible flow. These imply no thermal and compressibility effect. Hence, flow's behaviour is entirely described by the following equation set:

- Mass equation (according to incompressibility hypothesis)

$$\nabla \cdot \vec{V} = 0 \quad \text{Eq. 1}$$

Momentum equation

$$\frac{\partial \vec{V}}{\partial t} + \nabla \cdot \vec{V} \cdot \vec{V} = -\frac{1}{\rho_0} \nabla P + \nabla \cdot \nu \cdot \nabla \vec{V} \quad \text{Eq. 2}$$

$\vec{V}$  is the velocity vector,  $t$  the time,  
 $\rho_0$  the flow density,  $P$  the pressure, and  $\nu$  the cinematic viscosity.

### Numerical method

We now express briefly the numerical method. Our approach is similar to the numerical method used by Le Quéré and Gadoin in the natural convection flow instability studies (Le Quéré et al. 1992, Gadoin et al., 2001). Equations are discretized following a finite volume approach. Spatial discretization is carried out upon a non-regular structured staggered grid. Scalar variables are defined at cell centers whereas vectorial variables are defined at cells boundaries. The time derivative terms are approximated by a second order backward differentiation formula.

$$\frac{\partial f}{\partial t} = \frac{3f^{n+1} - 4f^n + f^{n-1}}{2\Delta t} + O(\Delta t^2) \quad \text{Eq. 3}$$

Superscripts  $n-1$ ,  $n$ , and  $n+1$  denote respectively the variable fields at times  $(n-1)\Delta t$ ,  $n\Delta t$  (known variables fields), and  $(n+1)\Delta t$  (unknown variable fields). To increase numerical stability, the viscous terms are explicitly defined at time  $(n+1)\Delta t$  and are spatially discretized with the classical second order centred scheme. The advection fluxes  $AF^n$  for each cell boundary of grid are calculated at time  $n\Delta t$  with the QUICK scheme - Quadratic Upstream for Convective Kinematics - (Leonard, 1979) and evaluated at time  $(n+1)\Delta t$  using the Adams-Bashford's extrapolation:  $AF^{n+1} = 2AF^n - AF^{n-1}$ . These different numerical schemes yield a Helmholtz type problem for the velocity. Discretized equations can be written for each control cell:

$$\left(\frac{2}{3\Delta t} I - \nu \nabla^2\right) \vec{V}^{n+1} = -\nabla P^{n+1} + S^n \quad \text{Eq. 4}$$

$$\nabla \cdot \vec{V} = 0$$

Where boundary conditions for  $\vec{V}$  are fixed values (Dirichlet conditions, except for the normal component of velocity at the outlet where we have adopted Neumann condition).  $S^n$  contains the sum of advection fluxes and terms of time derivative noted by superscripts n and n-1.  $\nabla^2$  and  $\nabla$  are respectively the discretized operators of laplacian and divergence.

Velocity-pressure coupling is carried out by the projection method based on Helmholtz's theorem. This yields Poisson's equation :

$$\nabla^2 \Phi = \rho_0 \frac{2}{3\Delta t} \nabla \cdot \vec{V}^{D*} \quad \text{Eq. 5}$$

With Neumann condition at domain boundaries for  $\Phi$  and  $\Phi = P^{n+1} - P^n + \nu \nabla \vec{V}^{D*}$

The pressure field  $P^{n+1}$  is calculated such as the velocity divergence is equal to zero (incompressibility hypothesis). For each time step, we have calculated the approximate solution  $\vec{V}^{D*}$  obtained from the Helmholtz equation (Eq.4), but where the pressure gradient term is defined at the time n  $\Delta t$ . Then, we have solved equation 5 to obtain  $\Phi$ . Eventually, the zero-divergence velocity field  $\vec{V}^{D^{n+1}}$  and the pressure field are updated:

$$\vec{V}^{D^{n+1}} = \vec{V}^{D*} - \frac{2\Delta t}{3\rho_0} \nabla \Phi$$

$$P^{n+1} = P^n + \Phi \quad \text{Eq. 6}$$

Helmholtz equations are integrated with A.D.I (Alternating Direction Implicit) method (Hirsh, 1988) whereas Poisson's equation is solved by the relaxed Gauss-Seidel method (Smith, 1985) coupled with a multigrid approach (P. Wesseling, 1992) to accelerate the convergence.

Boundary conditions are defined for velocity components as:

- Walls: No-sliding condition for tangential component of velocity, value fixed at zero for normal component.
- Inlet: Velocity profile is fixed according to experimental conditions. It has been numerically calculated from the laminar boundary layer growth that has been in agreement with experimental measurements carried out in the upstream cavity flow.
- Outlet: Normal velocity component gradient is equal to zero. Longitudinal velocity component is estimated with an "integrated characteristic" method such as mass conservation over the domain is warranted.

### Conditions of Simulations

We have performed five numerical simulations for different flow velocities varying from 0.8 m/s to 1.2 m/s with a step of 0.1 m/s. For each simulation, we have considered the domain corresponding to the median plane of the experimental flow. The domain is covered with 256 cells in the x-direction and 160 cells in the y-direction. The mesh is particularly refined close to walls and over the cavity in order to obtain a fine resolution concerning the upstream laminar boundary layer, the stress layer and eddy structures generated by instabilities. To minimize numerical inaccuracy, the greater size variation between successive cells is 5% (3% over the cavity) and the dimensional ratio for one cell is of the order of unity (maximum of 5 for further zones in regard to cavity). Each simulation is carried out in two steps: first, the statistical convergence of the flow is reached. Then, we have carried on simulation to calculate average variables of the flow and the temporal signal of longitudinal velocity component in specific points showed Figure 4. The period of signal recording is equal to  $2 \cdot 10^{-4}$  s. From temporal signal, defined by  $2^{15}$  recorded points, we have calculated Fourier transform to obtain the frequency spectrum. Results are discussed in the following section.

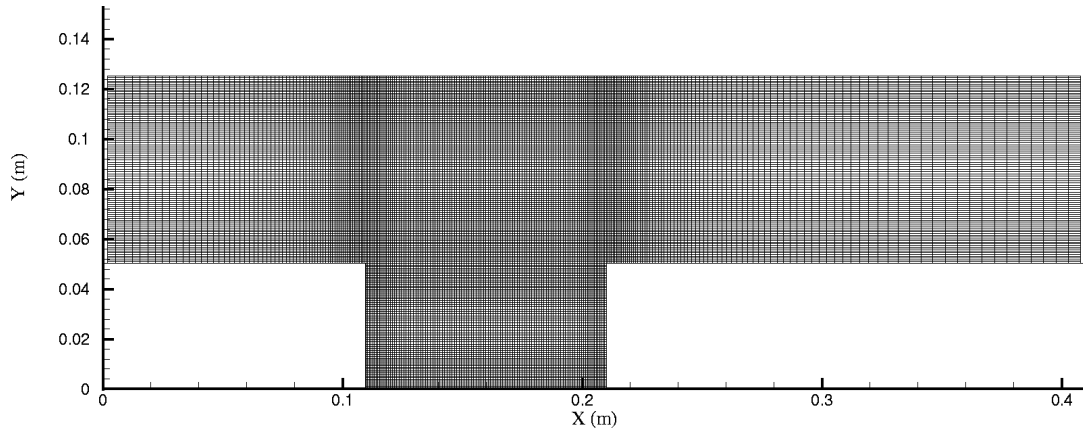


**Figure 3 :** Simulation grid 256x160 cells; the whole computation domain.

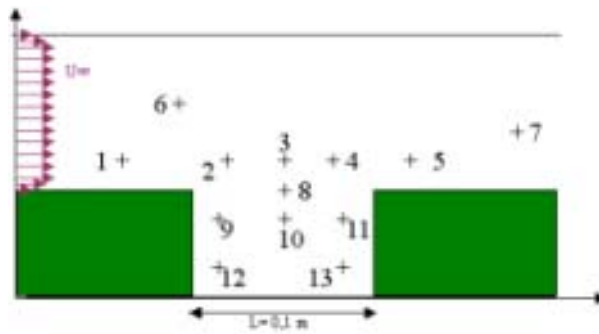


**Figure 4 :** Position of capture of time series in the DNS.

## RESULTS

The flow visualisation presented Figure 1, reveals the main features of the flow. The upward stream flow is separated from the vortex inside the cavity, by the shear layer. This layer is characterised by a development of instabilities growing as a billow of smoke, intermittently split by the downstream edge of the cavity. All these behaviours are clearly shown by the numerical simulation Figure 5. The splitting process at the downstream edge is especially well observed. It appears as a source of middle scale vorticity convected inside by the main vortex of the cavity.

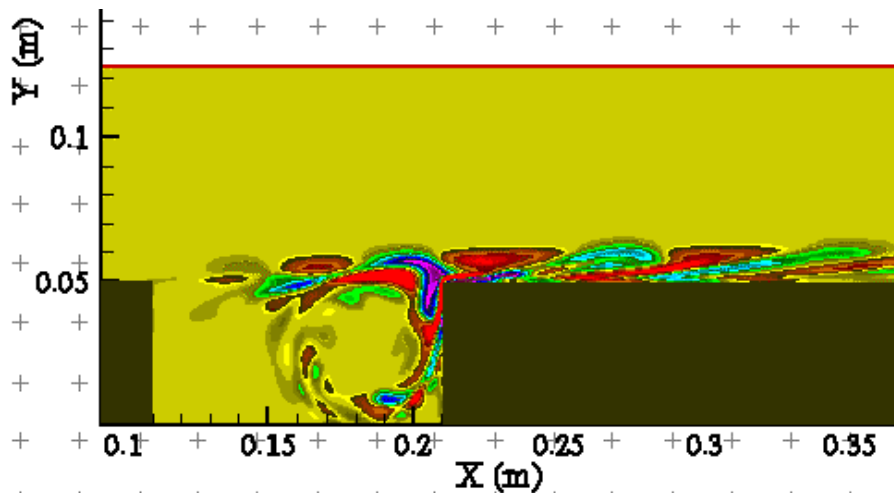


**Figure 5 :** 2D numerical simulation: visualisation of the iso-vorticity fluctuations.

## TEMPORAL DESCRIPTION

Let us consider Figure 6, the evolution of experimental power spectral density of energy, computed from the time series recorded in the shear layer ( $\sim$  point 5 of Figure 4), for increasing upstream flow rate. For  $U_\infty < 1.4 \text{ m/s}$  measurements exhibit 3 modes (mode 0, 1, 2). For  $U_\infty > 1.4 \text{ m/s}$  modes 0 and 1 disappear, mode 2 persists until 2.3 m/s and mode 3 appears. We can notice the existence of harmonics for some modes, but the study is limited to the fondamental frequencies.

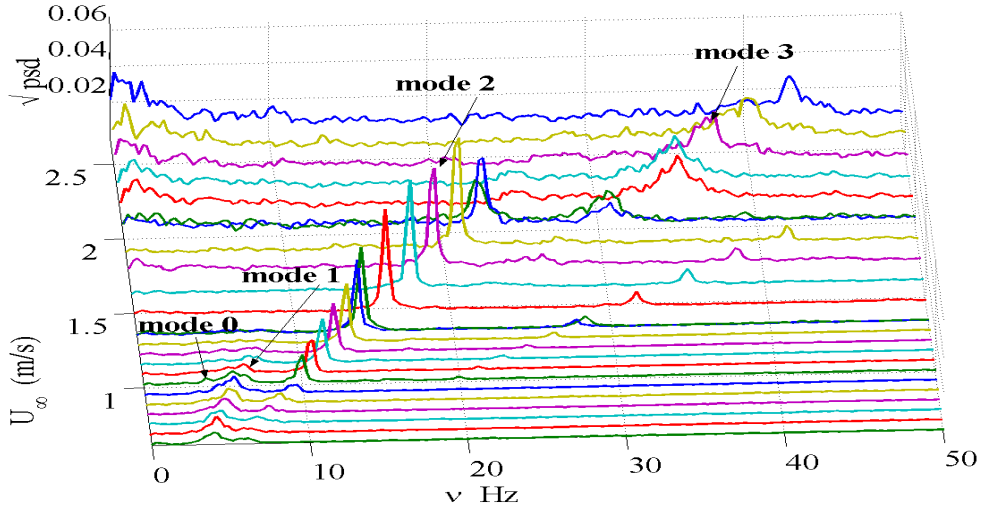


**Figure 6 :** Experimental power spectral density of energy from horizontal velocity component v.s. upstream flow rate:  $U_\infty \in [0.6, 2.6] \text{ m/s}$ .

It is interesting to follow the lines of maximum energy in the plane flow rate-frequency  $\{U_\infty, \nu\}$ . Figure 7 (upper part) gives the result for the modes 1 to 3 for the whole range of flow rate. The energy corresponding to each maximum line is also given Figure 7 (down part). In the domain of mode 3 the spectrum present a bright span ground of “noise”, which indicates that this mode belong to the weakly turbulent flow. The dynamic of the modes 1, 2, 3 exceed one decade.

In the range  $U_\infty \in [0.8, 1.2]$  power spectral density of energy are computed from time series catch at the points given Figure 4. For the point 13, the evolution of the spectrum with the flow rate is very similar to the experimental one, concerning the first 3 modes. Quantitative comparisons show the excellent agreement (Figure 9) in frequency values.

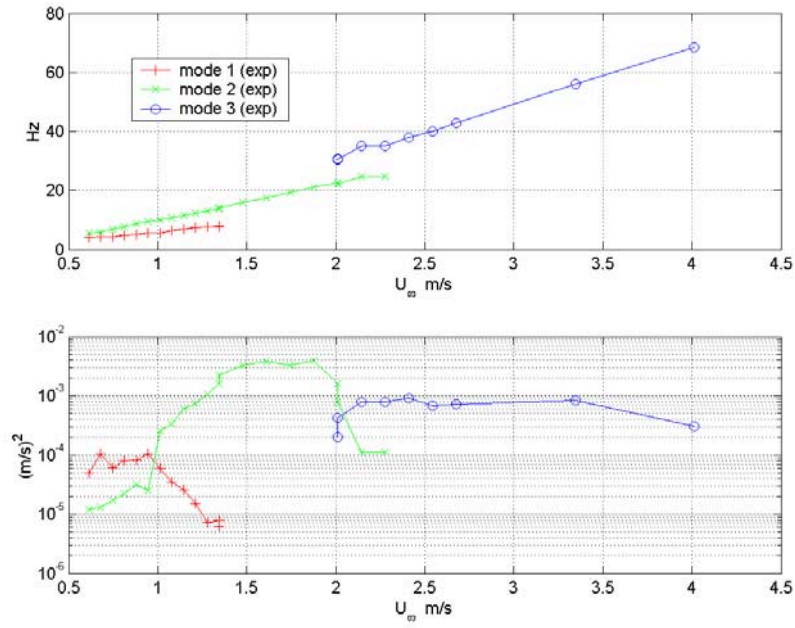


**Figure 7 :** Frequency modes (mode 0 is not represented) v.s upstream flow rate extended in the turbulent range of velocity  $U_\infty \in [0.6, 4.0]$  m/s (up). The corresponding energy of modes 1, 2, 3 are represented down.

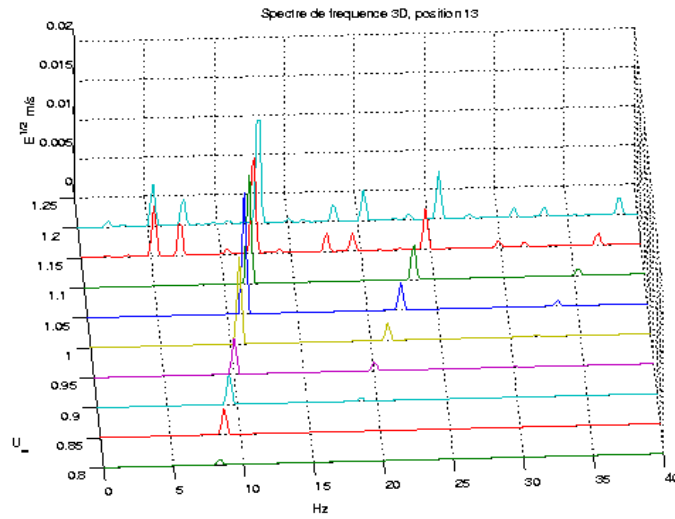


**Figure 8 :** DNS power energy spectrum from horizontal velocity component v.s. upstream flow rate:  $U_\infty \in [0.8, 1.2]$  m/s.

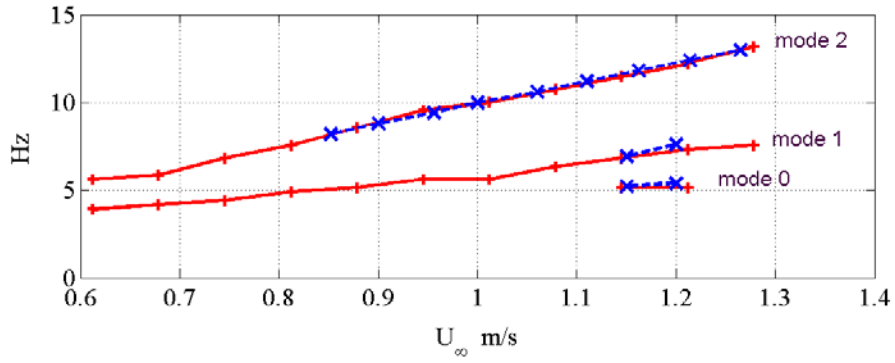


**Figure 9 :** Frequency modes v.s upstream flow rate: confrontation between numerical simulation (-x-) and experiment (-+-).

### SPATIAL DESCRIPTION

Figure 10 presents one image of the pair used to compute the velocity field. Let us remark that the billows of smoke, which correspond to emission lines, of course don't coincide with small vortex structures. Indeed, one main vortex and a small vortex at the upstream down edge mainly compose the flow inside the cavity. The zoom of the velocity field of the central part of the vortex (right part of Figure 10) allows us appreciating the spatial resolution given by the optical flow methods.

In previous temporal description is quoted that the spatial source of frequency mode 2 could be the shear layer instabilities. Therefore, in following will be focused on the extraction of a wavelength inside this shear layer. One notes that the vertical velocity component  $\mathbf{v}$  grows apparently linearly after the upstream edge of the cavity. This encourages us to identify the evolution of  $\mathbf{v}$  according to  $x$  with a physical description of instabilities growth  $\mathbf{v}(x) = a + be^{\beta x} \cos(2\pi x/\lambda + \varphi)$ . The fit is obtained using a two-dimensional unconstrained nonlinear minimisation (Nelder-Mead) with a linear regression at each step for the constants  $a$  and  $b$ . This procedure is applied on both experimental (Figure 11, left) and numerical (Figure 11, rights) profiles. The space amplification rates the wavelength obtained from experiment and simulation are in very good agreement (Tableau 1).

**Tableau 1:** Spatial amplification rate and wavelength.

	$\beta$	$\lambda$ (cm)
experimental	<b>28.7</b>	<b>5.77</b>
Numerical simulation	<b>27.8</b>	<b>5.56</b>

The relationship between the mode 2 and the shear layer instability is confirmed by the value  $c = \lambda/v \approx 0.42 \text{ m/s}$  for  $U_\infty = 0.85 \text{ m/s}$ . This celerity is very close to  $U_\infty/2$ , according to the linear stability analysis of a hyperbolic tangent profile [Godrèche (1996)].

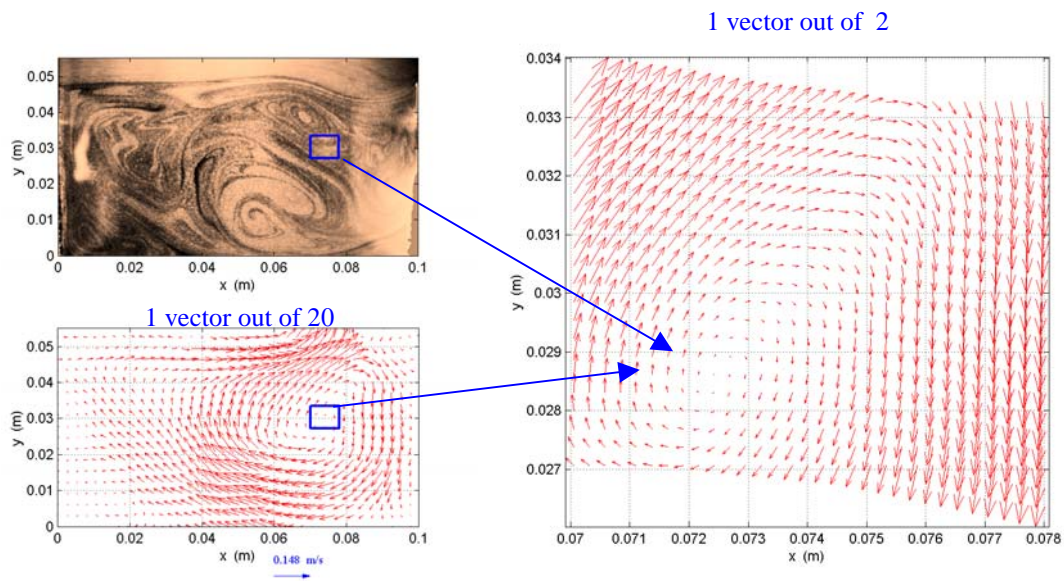


Figure 10 : Image of the seeded flow inside the cavity (up left) and 2D PIV, computed by optical flow : 1 vector out of 20 shown out of 20 computed (down left), 1 vector out of 2 (right).

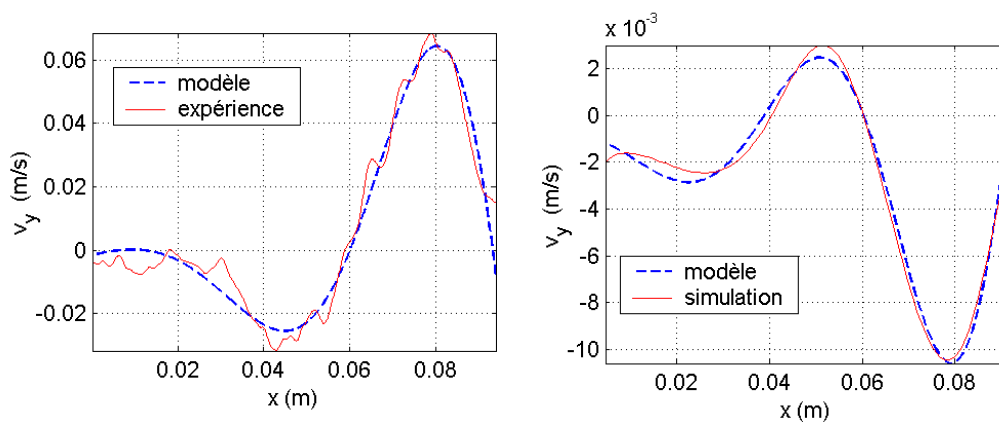
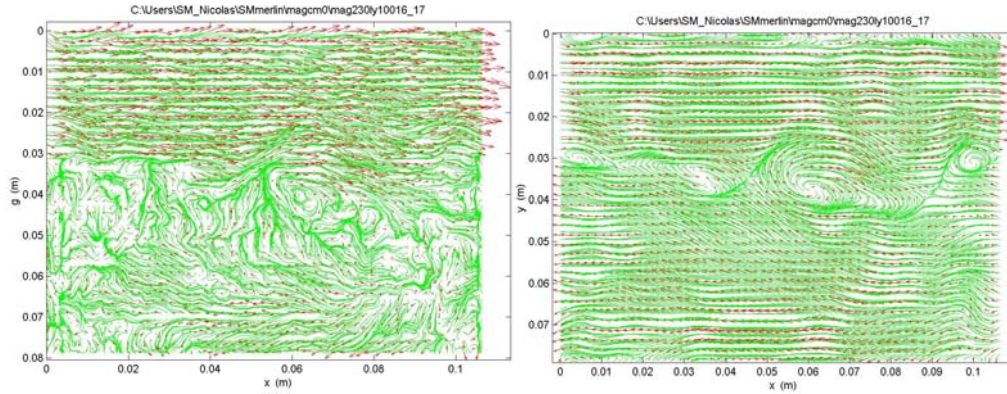


Figure 11 : Spatial mode identification on the vertical velocity component in the shear layer  $U_\infty = 0.85 \text{ m/s}$ .

Eventually, Figure 12 shows an example of the extraction of coherent structures, using a 2D Fourier filters, applied on both vertical and horizontal velocity matrices. In this case the scales above the tenth of the image size are kept. This operation leads to an information compression of 1 out of 40.



**Figure 12:** Coherent structure extraction from the velocity field obtained in weakly turbulent flow rate range; red arrows the velocity vectors, green lines the streamlines: initial velocity field (left), extracted shear layer instabilities.

In spite of the positive results mentioned above, the 2D DNS does not account of the mode 1 existence for the very low frequencies. Moreover the 2D DNS gives a pair of vortices in the cavity more symmetrical than the observation. Our first 3D DNS recently performed allow us to impute these limitations to the constraint imposed by the 2D simulation. Indeed, the non-symmetry of the main vortex inside the cavity could be attribute to the development of 3D spanwise instabilities.

#### REFERENCES :

- E. Gadoin, P. Le Quéré and O. Daube, « A general methodology for investigating flow instability in complex geometries : application to natural convection in enclosures “ Int. J. Num. Meth. Fluids, Vol 37, 175-208 (2001) .
- Ed. Godrèche and Manneville, “Hydrodynamics and non-linear Instabilities”, 1996, article from P. Huerre and M. Rossi.
- C. Hirsh, “Numerical computation of internal and external flows”, Vol 1: fundamentals of numerical discretization. eds. John Wiley & Sons – A Wiley Interscience Publication (1988).
- P. Le Quéré, R. Masson and P. Perrot., “A Chebyshev Collocation Algorithm for 2D Non-Boussinesq Convection”, J. Comput. Phys., Vol. 103, N°2 (1992).
- G.M. Quénot, J. Pakleza, T.A. Kowalewski, “Particle image velocimetry with optical flow”, *Exp. In Fluids* 25, 1998 pp177-189.
- B.P. Leonard,” A stable and accurate convective modelling procedure based on quadratic upstream interpolation, *Comput Methods in Applied Mechanics and Energy*, vol 19, pp 59-98, 1979.
- A. Rambert, A.Elcafsi, P. Gougat , « Optical flow velocimetry inside an entrained cavity », 10th Intl. Symp. on Appl. of Laser Techniques to Fluid Mechanics, Lisbonne Juillet 2000.
- G. D. Smith, “Numerical Solution of Partial Differential Equations – Finite Difference Methods”. Oxford Applied Mathematics and Computing Science series 3<sup>rd</sup> eds (1985).
- P. Wesseling, “An introduction to multigrid method”. John Wiley & Sons (1992).